Molecular Optimization for Nuclear Spin State Control via a Single Electron Spin Qubit by Optimal Microwave Pulses : Quantum Control of Molecular Spin Qubits

Molecular Optimization for Nuclear Spin State Control via a Single Electron Spin Qubit by Optimal Microwave Pulses: Quantum Control of Molecular Spin Qubits

Taiki Shibata, Satoru Yamamoto, Shigeaki Nakazawa, Elham Hosseini Lapasar, Kenji Sugisaki, Koji Maruyama, Kazuo Toyota, Daisuke Shiomi, Kazunobu Sato & Takeji Takui

Molecular Optimization for Nuclear Spin State Control via A Single Electron Spin Qubit by Optimal Microwave Pulses: Quantum Control of Molecular Spin Qubits

Taiki Shibata,[a] Satoru Yamamoto,[a] Shigeaki Nakazawa,[a, #] Elham Hosseini Lapasar,[a,b, *] Kenji Sugisaki,[a, c, d] Koji Maruyama,[a] Kazuo Toyota,[a] Daisuke Shiomi,[a] Kazunobu Sato[a]* and Takeji Takui[a,e,*]

[a] Department of Chemistry and Molecular Materials Science, Graduate School of Science, Osaka City University, Osaka 558-8585, Japan

[b] Department of Physics, University of Guilan, 41335-1914 Rasht, Iran

[c] JST PRESTO, Saitama 332-0012, Japan

[d] Centre for Quantum Engineering, Research and Education (CQuERE), TCG Centres for Research and Education in Science and Technology (TCG CREST), Kolkata 700091, India

[e] Research Support/URA Center, University Administration Division, Osaka City University, Osaka 558-8585, Japan

 # Deceased on March 23, 2019.

Corresponding author: Takeji Takui

E-mail address of the corresponding author: takui@sci.osaka-cu.ac.jp

Abstract

Quantum state control is one of the most important concepts in advanced quantum technology, emerging quantum cybernetics and related fields. Molecular open shell entities can be a testing ground for implementing quantum control technology enabling us to manipulate molecular spin quantum bits (molecular spin qubits). In well-designed molecular spins consisting of unpaired electron and nuclear spins, the electrons and nuclear spins can be bus and client qubits, respectively. Full control of molecular spin qubits, in which client spins interact via hyperfine coupling, is a key issue for implementing quantum computers (QCs). In solid-state QCs, there are two approaches to the control of nuclear client qubits, namely, direct control of nuclear spins by radio-wave (RF) pulses and indirect control via hyperfine interactions by microwave pulses applied to electron spin qubits. Although the latter is less popular in the literature, the indirectness has advantage of greatly reducing unnecessary interactions between a qubit system and its environment. In this work, we investigate molecular spin optimization to find optimal experimental conditions which can afford to achieve a high fidelity of quantum gates by the indirect control scheme. In the present quantum systems, one electron is directly controlled by pulsed ESR techniques without manipulating individual hyperfine resonance, but the states of two nuclear client spins are indirectly steered via hyperfine interactions. Single crystals of potassium hydrogen maleate (KHM) radical and ^{13}C-labeled malonyl radical are chosen as typical molecular spin qubits which exemplify the importance of the symmetry of hyperfine tensors and their collinear properties. We have found that both the non-collinearity of the principal axes of hyperfine coupling tensors and the non-distinguishability/non-equivalency between nuclear spins are key issues which extremely reduce the gate fidelity.

1. Introduction

Recently emerging quantum information science and relevant technology are expected to make some computational tasks, which are exceedingly hard to perform on a classical computer, achieve rather efficiently on a quantum computer [1]. Such applications will lead to a significant impact on chemistry, as well, from the estimation of precise molecular energies and wave functions to the deeper understanding of complex chemical reactions and properties, ultimately affording control or free manoeuver of such processes. In fact, the first quantum algorithm for full-CI calculations [2] appeared, which is based on a quantum phase estimation (QPE) algorithm [3]. The QPE algorithm renders the full-CI calculations executable on quantum computers in polynomial time against the system size of atoms and molecules. Furthermore, a novel quantum algorithm for full-CI calculations of open shell systems has been implemented recently [4]. The full-CI calculation for open shell chemical entities has been one of the most complex challenges in chemistry and physics, which are intractable with any classical computers.

Until recently, there have been a number of proposals as to how to configure quantum devices with various types of physical resources [5]. They make use of physical systems based on, e.g., linear optics [6], trapped ions [7-9], nuclear magnetic resonance (NMR) [10-12], electron spin resonance (ESR) [13], superconducting circuits [14-16], semiconductor quantum dots [17], to name but a few. In this work, we focus on molecular spin systems, in which electron and nuclear spins function as bus and client qubits, respectively. The electron spins are then controlled through pulsed microwave irradiations and they transfer quantum information to nuclear spins through electron-nuclear interactions [13, 18]. We term our spin system a molecular spin-based quantum computer (MSQC) symbolically. Although the number of spins in the system we manipulate in the laboratory is still rather limited, steering the quantum states of spin qubits at will is a challenging issue not only in implementing practical MSQCs [19-22] but also in terms of their molecular optimization in synthetic chemistry and materials science.

There are two major issues to be considered when attempting to realize prototypical MSQCs. The first one is to characterize the fundamental properties of open shell molecular entities as spin qubits, which govern their overall spin dynamics, i.e., the system Hamiltonian and the detail of the relaxation process. Both are relevant to current levels of microwave manipulation technology. Regarding the intrinsic nature of the Hamiltonian, the **g**, **A** (hyperfine coupling) and **D** (zero-field) tensor engineering have been investigated to optimize the spin orientations with respect to the static magnetic field and the spin interaction strength in open shell organic molecules [12, 24, 25] and metal complexes [26]. At the same time, a great deal of effort has been made to understand their relaxation process, to specify relevant parameters such as the spin–lattice relaxation time to establish pseudo initialization conditions, and to make the coherence time elongated with respect to the spin interaction strength to benefit from quantum mechanical effects on gate operations for quantum information processing and quantum computing (QC) as much as possible [22, 27-30].

The other major issue is the precise control of multiple spins, which is the core technology of

quantum information processing and QC. The spin qubits of MSQCs are in principle controlled by pulse-based microwave/ESR techniques, which can afford the counterparts of NMR-based spin operations [18, 31, 32]. In fact, the experiments of MSQCs have already been performed with rectangular pulses to implement various gate operations [13, 19-26, 30, 31]. The recent advance in technology, however, has made arbitrary wave generators (AWGs) available in the field of pulsed microwave/ESR spectroscopy, enabling us to manipulate molecular spins with arbitrary pulse profiles in a desired manner [31-33]. This gives us more degrees of freedom in controlling the spin dynamics of molecular multiple spin-qubit systems in various schemes.

As we will see below, quantum operations are applicable to appropriate molecular spin systems, which consist of both electron and nuclear spins, by modulating the interaction field of microwave that couples the electron with the nuclear spins. In this scheme, the nuclear spins are indirectly manipulated through the electron spin. We emphasize that the full controllability through the indirect access can be checked mathematically by looking into the system Hamiltonian. Once we have verify the controllability, the next step is to compute pulse shapes to implement given operations. To this end, there are two standard approaches, namely, Krotov algorithm [36] and Gradient Ascent Pulse Engineering (GRAPE) [37]. While Krotov algorithm optimizes a pulse intensity stepwise in time, GRAPE changes the entire pulse profile at once. In experiments for NMR-based QCs, quantum algorithms have been executed by using GRAPE pulses applied to homonuclear spin systems [38, 39]. GRAPE pulses have also been employed in order to control the molecular spin system of malonyl radical, whose electron and nuclear spins are coupled through hyperfine interactions [40, 41]. Furthermore, it is also applicable to the cases in which microwave field strength is strong ($Q > 10000$: Q denotes the quality factor as a measure of the radiation loss in a resonator and gives the radiation field strength), demonstrating the occurrence of the improved GRAPE optimization [42].

In this work, we investigate how molecular spin characteristics affect the effectiveness of quantum control, especially when we control a multiple spin system indirectly through a small gateway. More specifically, we consider physical situations in which we attempt to apply arbitrary unitary operations on a three-spin system, consisting of two nuclear and one unpaired electron spins, by manipulating the electron spin with microwave irradiation. Molecular spin qubits as testing grounds are potassium hydrogen maleate (abbreviated as KHM) radical and ^{13}C-labeled malonyl radical. They have different spin structures and serve as models of different spin dynamics [43, 44]. Since our primary interest here is the fundamental controllability, we focus on the unitary evolution of a closed system, neglecting any spin relaxation processes in the spin systems under study. Nevertheless, when designing the optimal pulses, the operation time is set to be sufficiently short so that the designed pulses would be practically useful in the laboratory.
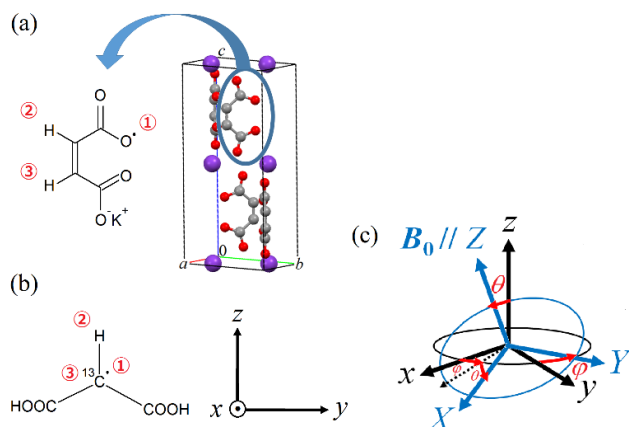
Fig. 1 Molecular spin systems with the computational coordinates, *XYZ* and molecular principal axes, *xyz*. (a) A molecular structure of KHM radical and its Cartesian coordinates (*abc*) in the single crystal, where the crystallographic axes are denoted by *abc* . Red, grey and purple spheres represent ^{16}O, ^{12}C and ^{39}K nucleus, respectively. An unpaired electron, $^1H2$ and $^1H3$ spins are utilized as the 1st, 2nd and 3rd qubit shown as the numbers in red circles, respectively. The unpaired electron is delocalized over the molecule. (b) A molecular structure of ^{13}C-labeled malonyl radical. An unpaired electron, ^1H and ^{13}C spins are utilized as the 1st, 2nd and 3rd qubit shown as the numbers in red circles, respectively. Coordinates (*xyz*) designate the principal axes of the hyperfine tensor of ^1H as the α-proton. Note that speaking exactly the molecular structure of malonyl radical itself in the host crystal lattice of malonic acid has not fully been determined in its crystal structure, to our knowledge. The optimized molecular structure of malonyl radical in the crystal lattice of malonic acid is given in Supporting Information (4). The optimized structure of malonyl radical in the crystal lattice has been obtained by considering sixteen host molecules surrounding malonyl radical in the lattice. (c) The definition of the computational coordinates, *XYZ* with respect to the *xyz* coordinates. The angles, *φ* and *θ* are defined as Euler angles. The static magnetic field B_0 is oriented along the *Z* axis.

2. Theory

2.1 Controllability of spin systems

The controllability of spin systems under study can be verified by examining the Lie algebra generated by spin Hamiltonians which fully describe the multiple spin states. The spin systems adopted in this work can be described in terms of the Hamiltonians given in Eqs. (3) and (4) [45, 46]. For the specific systems considered below, it is shown that any unitary operations in SU(2^N), where N is the number of spin-1/2, can be realizable by modulating H_{ctrl} [41, 47], hence they are fully controllable except for some special cases: H_{ctrl} is a time-dependent Hamiltonian termed a control Hamiltonian, as shown in Eq. (4).

From such an algebraic analysis, we can see that what contributes to the controllability is the non-commutativity of component Hamiltonians, e.g., $[H_0, H_{ctrl}]$, $[H_0,[H_0, H_{ctrl}]]$, etc. These new operators that appear as a result of taking commutators lead to unitary operations that might look nontrivial at the first sight. Therefore, intuitively, in order to have as many effective Hamiltonians as possible, they should have substantial off-diagonal terms that lead to non-commutativity between them. For the same reason, the more anisotropic the system, the better not to have any preferred direction in the space. The importance of the off-diagonal terms and anisotropy will manifest in the following sections: It is worth noting that the magnitude of the anisotropy of the magnetic properties of spin systems is relevant to the fidelity of quantum gates.

2.2 Quantum state control in MSQCs

Quantum dynamics in a closed system (any spin relaxations not considered) is governed by Hamiltonian of the system ($H(t)$), since the time evolution operator $U(t)$ is described by Schrödinger equation, as given in Eq. (1). In the quantum control theory, Hamiltonian $H(t)$ is split into two terms (Eq. (2)), i.e. H_0 and $H_{ctrl}(t)$. The former one is the drift Hamiltonian that permanently acts on the system, and then quantum states are manipulated by adjusting the control parameters of the latter control Hamiltonian.

$$i\frac{d}{dt}U(t) = H(t)U(t), \qquad U(0) = I \tag{1}$$

$$H(t) = H_0 + H_{ctrl}(t) \tag{2}$$

A field-free and unperturbed Hamiltonian H_0, called the drift Hamiltonian, describes the intrinsic spin dynamics of open shell molecules, which is time-independent in the rotating frame of electron spins after applying a secular averaging approach (SAA). The drift Hamiltonian H_0 models the dynamics of the spin system and denotes an uncontrolled part of the Hamiltonian, called "drift". As seen below, importantly microwave with a single frequency ($\nu_{MW}/2\pi$) and its time-dependent amplitude ($\nu_1(t)$) is sufficient to control one electron bus qubit and two nuclear client qubits. Thus, two Hamiltonian components in the laboratory frame (XYZ) can be simply described as follows:

$$H_0 = \Delta v_0 S_Z - \gamma_{n1} B_0 I_Z^1 - \gamma_{n2} B_0 I_Z^2 + \sum_{i \sim X,Y,Z} A_{Zi}^1 S_Z I_i^1 + \sum_{i \sim X,Y,Z} A_{Zi}^2 S_Z I_i^2 \qquad (3)$$

$$H_{ctrl}(t) = v_1(t) S_X \qquad (4)$$

Here, Δv_0 is the frequency offset between Larmor and the microwave frequency of the electron spin, and the static magnetic field B_0 is applied along the Z-direction. γ_{nk} and A^k are the nuclear gyromagnetic ratios and the hyperfine tensor to the k-th nucleus, respectively.

Table 1 Relations between the principal axes of hyperfine tensors and the low fidelity points. The symbols φ and θ denote Euler angles defined in **Fig. 1**(c). The fidelity of a quantum gate is defined by Eq. 5.

a) KHM radical

Interaction with	Orientations of the static magnetic field (φ /°, θ /°)	Low fidelity points
2nd qubit (^{1}H2)	(50, 90)	(1)
2nd qubit (^{1}H2)	(139, 30)	(4)
2nd qubit (^{1}H2)	(140, 120)	(5)
3rd qubit (^{1}H3)	(50, 90)	(1)
3rd qubit (^{1}H3)	(140, 60)	(2)
3rd qubit (^{1}H3)	(139, 150)	(3)

b) ^{13}C-labeled malonyl radical

Interaction with	Orientations of the static magnetic field (φ /°, θ /°)	Low fidelity points
2nd qubit (^{1}H)	(0, 0)	(6)
2nd qubit (^{1}H)	(0, 90)	(7)
2nd qubit (^{1}H)	(90, 90)	(8)
3rd qubit (^{13}C)	(127, 175)	(6)
3rd qubit (^{13}C)	(0, 93)	(7)
3rd qubit (^{13}C)	(90, 86)	(8)

2.3 Optimization of microwave pulses by the GRAPE method

In order to find conditions of the molecular optimization appropriate to the quantum control of spin qubits, we first need to optimize the control pulses to implement a given unitary operation U_{target}. In our approach, the total duration of an operation is prefixed at T and then the modulation of the microwave magnetic field is so designed as for the resulting time evolution operator $U(T)$ to be as close to U_{target} as possible. The distance between the two operators can be evaluated by the fidelity f defined as

$$f = \frac{1}{N}\left|tr\left\{U_{target}^{\dagger}U(T)\right\}\right|$$
(5)
.

where N is the number of spin-1/2 particles. The fidelity f is by definition in the range of $0 \leq f \leq 1$; f equals 1 when $U(T)$ is identical to U_{target} up to a global phase.

Table 2 Typical conditions in the GRAPE simulations. The parameters were selected so as to carry out ESR experiments and qualify the GRAPE pulses.

Magnitude of B_0	1.1 T (Q-band)
Offset frequency, Δv_0	10 MHz
Computational time step, Δt	5 ns
Operation time for KHM radical	0.5 μs
Operation time for malonyl radical	0.3 μs

When optimizing the GRAPE pulses, we have utilized the DYNAMO package, which is a toolbox developed to run on Matlab [48]. For a given T and U_{target}, it optimizes the amplitude $v_1(t)$ of H_{ctrl} as a function of time, using the Broyden-Fletcher-Goldfarb-Shanno (BFGS) method [49]. In this method for optimizing the GRAPE pulses, the time profile of $v_1(t)$ over $[0,T]$ is optimized simultaneously for all time steps during the duration T, unlike other methods such as Krotov's [37]. As a result, the process tends to give a higher probability in finding more optimal pulse profiles, which is recommended by DYNAMO.

2.4 The molecular spin systems and spin interaction parameters

We have selected two types of molecular spin qubits for our analysis, namely potassium hydrogen maleate (KHM) radical [43, 50] and ^{13}C-labeled malonyl radical [30, 44]. The reason for the selection is that they have different molecular symmetries, nuclear species of different nuclear quantization axes, and axial properties of their hyperfine tensors, leading to different sets of hyperfine spin

Hamiltonians. Their salient features give us key elements to implement indirect optimal control in molecular spin qubits from the viewpoint of quantum cybernetics. In other words, in this choice both molecular spins have significant off-diagonal terms of the hyperfine tensors in a different way. Moreover, they have been known as a robust sample for ESR experiments at ambient temperature, thanks to the easiness of magnetic dilution and reasonably strong ESR signals of their single crystals in desired orientations with respect to the static magnetic field.

KHM radical has a symmetric molecular configuration, whose molecular structure is of C_{2v} symmetry in the orthorhombic crystal (Fig. 1a) [43]. The unit cell contains two pairs of KHM molecules, i.e., the four molecules, and each pair can be regarded independent because the magnetic dilution makes the inter-pair interaction negligible. In our sample, signals attributable to the formation of intermolecular triplet spin species have not been observed. Thus, we focus on a single pair of the molecules (encircled in blue in Fig. 1a) for our analysis. The two pairs are only crystal-symmetry related and magnetically distinguishable.

The electron spin and the two nuclear spins of ^{1}H2 and ^{1}H3 nuclei are utilized as the 1st, 2nd and 3rd qubits, respectively. The hyperfine tensors used for theoretical simulations in the *abc* crystallographic coordinates (note that *xyz* denote Cartesian molecular coordinates as depicted in Fig. 1a) are given as follows [48]:

$$A_{\mathrm{KHM}}(\mathrm{H2})=\begin{pmatrix} -14.6 & -3.7 & 7.4 \\ -3.7 & -16.0 & -6.3 \\ 7.4 & -6.3 & -23.0 \end{pmatrix} \mathrm{MH}z \tag{6}$$

$$A_{\mathrm{KHM}}(\mathrm{H3})=\begin{pmatrix} -14.6 & -3.7 & -7.4 \\ -3.7 & -16.0 & 6.3 \\ -7.4 & 6.3 & -23.0 \end{pmatrix} \mathrm{MH}z \tag{7}$$

The above hyperfine tensors with different signs of the off-diagonal elements have the same principal values and they share one of the principal axes.

On the other hand, ^{13}C-labeled malonyl radical depicted in Fig. 1b has a very notable property in terms of the hyperfine tensors: The principal axes of the hyperfine tensors of the ^{13}C and α-proton are nearly the same [44]. Since malonyl radical is in a triclinic crystal system, the single crystal gives only one kind of molecular species in any orientation of the static magnetic field with respect to the crystal. Having set the molecular coordinate (*xyz*) to match the principal axes of the α-proton, the hyperfine tensors can be expressed as [28, 30]

$$A_{\mathrm{mal}}(^1\mathrm{H})=\begin{pmatrix} -56.0 & 0.0 & 0.0 \\ 0.0 & -91.5 & 0.0 \\ 0.0 & 0.0 & -26.6 \end{pmatrix} \mathrm{MH}z \tag{8}$$

$$A_{\mathrm{mol}}\left(^{13}\mathrm{C}\right)=\begin{pmatrix} 211.8 & 1.0 & -8.9 \\ 1.0 & 24.6 & -1.3 \\ -8.9 & -1.3 & 43.4 \end{pmatrix} \mathrm{MHz} \tag{9}$$

The relation between the laboratory frame (*XYZ*), in which the static magnetic field B_0 and the microwave field are applied, and the molecular coordinate (*xyz*) are shown in Fig. 1c. We define the molecular orientation by Euler angles (φ, θ) as shown in the figure and the directions of the principal axes are shown in Table 1.

2.5 Conditions for microwave pulse optimization

In the optimization based on the GRAPE algorithm, both the angles φ and θ, which denote the direction of the static magnetic field, are swept over the half sphere, i.e., $\varphi, \theta \in [0°, 180°]$, with an increment of 5 degrees for each angle. The 5 degrees gave enough space resolution in our simulation. The other parameters, such as computational time steps, the operation time of a quantum gate, the strength of the static magnetic field B_0, and the offset frequency Δv_0 of microwave, are fixed in the computation as given in Table 2. The last two parameters, B_0 and Δv_0, are chosen to give a high fidelity after a crude search for the near-optimal values of them (See Supporting Information). Other conditions which alternatively give lesser fidelity are also discussed in Supporting Information. The target quantum gates U_{target} as described in a matrix form are in the following:

$$\mathrm{CNOT1}=\begin{pmatrix} 1 & 0 & 0 & 0 & 0 & 0 & 0 & 0 \\ 0 & 1 & 0 & 0 & 0 & 0 & 0 & 0 \\ 0 & 0 & 0 & 1 & 0 & 0 & 0 & 0 \\ 0 & 0 & 1 & 0 & 0 & 0 & 0 & 0 \\ 0 & 0 & 0 & 0 & 1 & 0 & 0 & 0 \\ 0 & 0 & 0 & 0 & 0 & 1 & 0 & 0 \\ 0 & 0 & 0 & 0 & 0 & 0 & 0 & 1 \\ 0 & 0 & 0 & 0 & 0 & 0 & 1 & 0 \end{pmatrix} \tag{7}$$

$$\mathrm{CNOT2}=\begin{pmatrix} 1 & 0 & 0 & 0 & 0 & 0 & 0 & 0 \\ 0 & 0 & 0 & 1 & 0 & 0 & 0 & 0 \\ 0 & 0 & 1 & 0 & 0 & 0 & 0 & 0 \\ 0 & 1 & 0 & 0 & 0 & 0 & 0 & 0 \\ 0 & 0 & 0 & 0 & 1 & 0 & 0 & 0 \\ 0 & 0 & 0 & 0 & 0 & 0 & 0 & 1 \\ 0 & 0 & 0 & 0 & 0 & 0 & 1 & 0 \\ 0 & 0 & 0 & 0 & 0 & 1 & 0 & 0 \end{pmatrix} \tag{8}$$

$$\mathrm{SWAP1}=\begin{pmatrix} 1 & 0 & 0 & 0 & 0 & 0 & 0 & 0 \\ 0 & 0 & 1 & 0 & 0 & 0 & 0 & 0 \\ 0 & 1 & 0 & 0 & 0 & 0 & 0 & 0 \\ 0 & 0 & 0 & 1 & 0 & 0 & 0 & 0 \\ 0 & 0 & 0 & 0 & 1 & 0 & 0 & 0 \\ 0 & 0 & 0 & 0 & 0 & 0 & 1 & 0 \\ 0 & 0 & 0 & 0 & 0 & 1 & 0 & 0 \\ 0 & 0 & 0 & 0 & 0 & 0 & 0 & 1 \end{pmatrix} \tag{9}$$

The basis in these matrices are aligned as $|\uparrow\uparrow\uparrow\rangle$, $|\uparrow\uparrow\downarrow\rangle$,..., $|\downarrow\downarrow\downarrow\rangle$. CNOT1 in Eq. (7) is a controlled-NOT operation that flips the spin state of the 3rd qubit as the target qubit when the 2nd qubit as the controlled qubit is in the spin down $|\downarrow\rangle$ state. CNOT2 has a similar effect, but flips the second spin qubit, conditional on the spin state of the third qubit. SWAP1 swaps the states of the two nuclear client spins.

3. Results and discussion

3.1 Gate operations on KHM radical in the single crystal

Figure 2 shows the results of the fidelity optimization for the three types of quantum gates, i.e., CNOT1, CNOT2 and SWAP1. The calculated optimal fidelity is plotted as a function of the molecular orientation defined by Euler angles, φ and θ. There are some areas where the fidelity is considerably low, indicating that there is an apparent limitation on the controllability.

As seen in Fig. 2, there are five (four small and one large) bright spots, where their fidelity is considerably low: All the five spots are evident in Fig. 2(c). These spots correspond to the orientations along the principal axes of the two hyperfine tensors of the hyperfine qubits, ^{1}H2 and ^{1}H3 of KHM radical. The orientation of $\varphi = 50°$, $\theta = 90°$ corresponds to the co-principal axis of the hyperfine tensors of the two nuclei, which can be calculated from Eq. (3) (see Table 1). For the CNOT1 operation, all the orientations, including the one for Spot (1) at $\varphi = 50°$, $\theta = 90°$, revealing low fidelity appearing in Fig. 2, and the corresponding hyperfine elements, (A_{ZX}, A_{ZY}, A_{ZZ}) of both the control and target hyperfine qubits are summarized with their fidelity in Table 3. Only in the gate operation of CNOT1, Spots (4) and (5) gave 0.99 of the fidelity.

Besides the five spots, there are two lines, one at $\varphi = 50°$ and the other one at $\theta = 90°$, where the fidelity is lower than in the other areas for CNOT1 and CNOT2. In Table 3, the hyperfine elements corresponding to the two lines, as denoted by α and β, are also given. As a reference of the fidelity, the hyperfine elements at an orientation ($\varphi = 10°$, $\theta = 150°$), which is far from the areas with low fidelity, are given for comparison. Below we discuss the mechanism which governs the fidelity and why the molecular orientations corresponding to the above five spots and the particular two lines fail to get high fidelity.

Table 3 Orientation dependence of the fidelity of CNOT1 gate for KHM radical on the hyperfine tensor elements, where H2 is the control hyperfine qubit and H3 the target hyperfine qubit. The hyperfine elements for H2 and H3 at a given orientation are written in the upper and lower row, respectively.

Orientation		Hyperfine tensor element/MHz			Fidelity
Properties	$(\varphi\ /°, \theta\ /°)$	AZX	AZY	AZZ	
Reference	(10, 150)	0.0	4.6	-26.6	0.99
		-6.2	-8.3	-15.9	
Spot (1)	(50, 90)	0.0	-0.1	-19.0	0.30
		-0.0	-0.1	-19.0	
Spot (2)	(140, 60)	9.8	0.1	-22.8	0.50
		0.1	0.0	-6.0	
Spot (3)	(140, 150)	-9.8	0	-11.7	0.50
		-0.1	0.1	-28.5	
Spot (4)	(140, 30)	0.1	0.1	-28.5	0.99
		9.8	0	-11.7	
Spot (5)	(140, 120)	-0.1	0.0	-6.0	0.99
		-9.8	0.1	-22.8	
Line (α)	(50, 30)	1.7	-8.4	-22.1	0.75
		1.7	8.4	-22.0	
Line (ß)	(140, 90)	9.7	0.1	-11.5	0.75
		-9.7	0.1	-11.5	
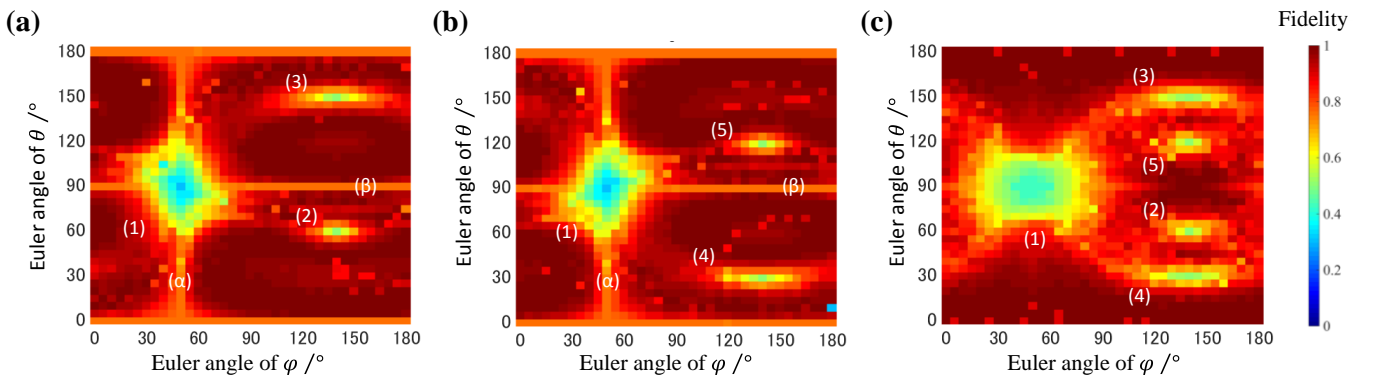
Fig. 2 Contour plots of the optimized fidelity distribution of KHM radical in the crystal as a function of Euler angles, φ and θ, which define the molecular orientation. For a given orientation (φ, θ), the maximum reachable fidelity of the operation is plotted. The orientations denoted by the numbers from (1) to (5) give particular low fidelity. (a) CNOT1 gate. (b) CNOT2 gate. (c) SWAP1 gate.

Referred to the gate operation of CNOT, the information on the control qubit state is merely read and its state is not subject to active control. Thus, the interaction between the electron and the control qubit nucleus is used only to read out the state of the latter, that is, the off-diagonal components in the hyperfine tensor of the control hyperfine qubit are not necessarily requisites for the operation. Although it sounds somewhat counterintuitive, it can be understood by considering a diagonal two-spin Hamiltonian of the form $Z \otimes I + Z \otimes Z$ collinear, where Z and I denote Pauli Z and unit matrixes, respectively. Obviously, the dynamics of the first spin depends on the second one, and thus the state of the second spin can be read out.

On the other hand, in order to control the target qubit the off-diagonal elements are necessary to efficiently flip it. This can be observed in Fig. 2; the spots 2 and 3 along the $\varphi = 140°$ line in Fig. 2a correspond to the condition which makes the off-diagonal elements in the hyperfine tensor for the H3 (target qubit) vanishing. Because of the non-equivalence of the principal axes of the hyperfine qubits, the two spots, 4 and 5, appear at different directions when the control and the target qubits are exchanged during the CNOT2 gate operation as in Fig. 2b. At the largest spot 1 in Figs. 2a and 2b, the hyperfine qubits share the common principal axis, hence the fidelity is low in both the above cases. The same feature can be seen in Table 3. In the case of the SWAP operation for the two nuclear spins, all five spots appear in the plot of fidelity in Fig. 2c, since it entails spin rotations for both the hyperfine qubits.

For the orientations $\varphi = 50°$ and $\theta = 90°$ on the two lines α and β, however, the off-diagonal components of the hyperfine tensor are not close to zero, except for the crossing points of the two line. The reasons are in the following. First we focus on the line $\theta = 90°$, and for the other line $\varphi = 50°$ the reason can be explained in a similar manner.

Recall that the contour plot in Fig. 2a is represented as a function of the direction of the principal axes, in which the hyperfine tensor for the H2 hyperfine qubit is diagonalized. This is also obvious for the plot in Fig. 2b (for the H3 hyperfine qubit). The two qubits are structurally correlated by C_{2v} symmetry and the principal values are the same. This implies that at the point (φ, θ), which is in the middle of the two spots, 2 and 5, the hyperfine tensors have essentially the equal values, modulo their signs. In other words, the point (φ, θ) can be reached from the spots 2 and 5 by rotating the coordinate by the same angle (but around the different rotation axes). The set of such points forms a line of either $\varphi = 50°$ or $\theta = 90°$. From the viewpoint of the indirect control via the electron spin, it is then hard to distinguish between the dynamics of the two hyperfine qubits, because both react to the signal from the electron spin in the same way. Therefore, the fidelity of operations becomes lower on the lines α and β. The lines look dimmer in Fig. 2c, because roughly speaking the two hyperfine qubits can be dealt with equally in the case of the SWAP operation.
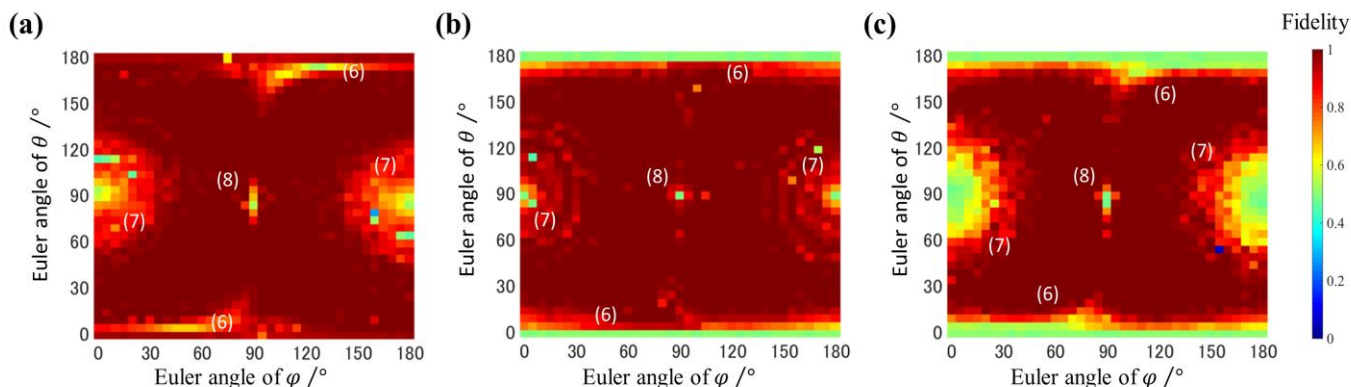
Fig. 3 Contour plots of the Optimized fidelity distribution of the ^{13}C-labeled malonyl radical as a function of Euler angles, φ and θ, which define the molecular orientation. For a given orientation (φ, θ), the maximum reachable fidelity of the operation-is plotted. The orientations denoted by the numbers from (1) to (5) give particular low fidelity. (a) CNOT1 gate. (b) CNOT2 gate. (c) SWAP1 gate.

3.2 Gate operations on malonyl radical in the crystal

The hyperfine tensors for the α-proton (2nd qubit) and the ^{13}C (3rd qubit) nucleus of ^{13}C-labeled malonyl radical have approximately the same principal axes and they are nearly collinear. This property minimizes the number of spots (in the (φ, θ)-plane) which correspond to very low fidelity for the gate operations. The fidelity distribution as a function of the direction of the static field is presented in Fig. 3. The off-diagonal elements of the hyperfine tensors vanish when the field is applied along one of the principal axes, whose directions are in (φ, θ) = (90°, 90°), $\theta = 0°$, and $\theta = 180°$.

Since the two nuclear species are different, they are always distinguishable in the gate operation by using malonyl radical in the crystal. Thus, the straight lines, which are visible in Fig. 2 as a result of coincidence of the tensors for the two hyperfine qubits, do not appear in Fig. 3.

Consequently, the overall gate fidelity with malonyl radical is higher over the entire region of (φ, θ) except for a few directions than that with KHM radical. Thus, for the purpose of indirect quantum control of molecular spins, malonyl radical offers a more suitable test bed than KHM radical, suggesting useful guidelines for molecular optimization and characteristics in quantum control experiments.

3.3 Optimal conditions for molecular spin quantum control with GRAPE algorithm

Now that we have found that malonyl radical provides us with a good test bed for indirect quantum control in molecular spin qubits, we discuss the optimal condition for the indirect control (Fig. 3a and 3b). Figure 3c suggests that the orientations far from the directions of the principal axes give the higher fidelity. This is true as far as we confirmed the situations in the numerical calculations. Typically, the four directions, (45°, 45°), (45°, 135°), (135°, 45°) and (135°, 135°), lead to the highest fidelity.

As an example, a numerically obtained GRAPE pulse for CNOT1, executing the gate

operation at $(\varphi, \theta) = (45°, 45°)$, is shown in Fig. 4. As the four directions are all equivalent, giving $f = 0.99$ for three types of the unitary operations under study, the results are essentially for the optimal condition.

Figures 4c and 4d exemplify the optimal two pulses obtained with $f = 0.99$ and the different length, respectively. The former one was generated by the standard condition used in Fig. 3, in which a strong control oscillating magnetic field (>100 MHz) is applied. Taking account of the limit of the feasible field strength (< 25 MHz) available in conventional experimental setups, the latter optimal pulse is feasible from the experimental side with the elongation of the pulse length from 0.3 to 1.2 μs.
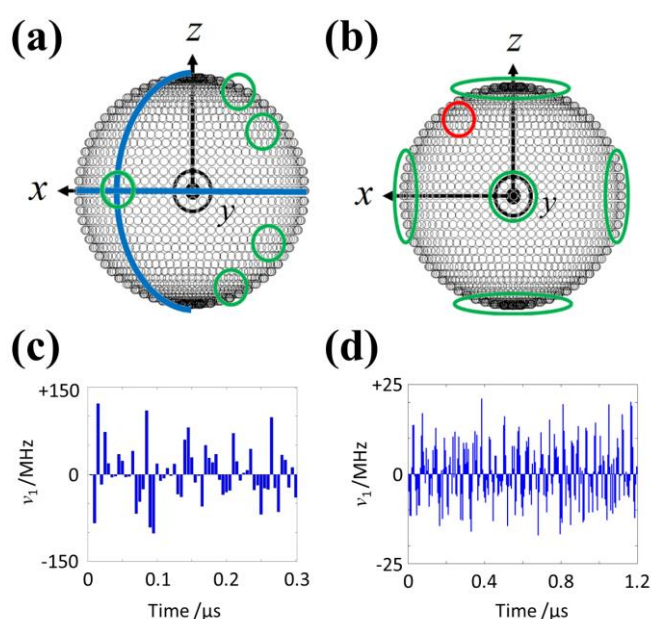
Fig. 4 Plots of the fidelity and GRAPE pulse for experiments for (a) KHM radical and (b) ^{13}C-labeled malonyl radical. A black circle in (a) and (b) denotes the direction of the static magnetic field (B_0 // Z) direction. Blue lines, green circles and a red circle denote the directions for the occurrence of the symmetric hyperfine elements, the directions of the hyperfine principal axes and an optimal molecular orientation, respectively. In (c) and (d) are shown the optimal pulses (Q-band GRAPE pulse) for CNOT1 at the optimal molecular orientation. The operation time is 0.3 μs for (c) and 1.2 μs for (d).

3.4 Importance of GRAPE algorithm in quantum control

It is worth noting that spin-qubit based QC implementations have been carried out from the viewpoint of spin Hamiltonian engineering, which enables us to access each molecular spin by conventional rectangular microwave/radio wave pulses for quantum gates, and the relevant *g*- and *A*-tensor engineering approaches have dealt with the first experiment on demonstrating the spinor property of an electron spin, CNOT gate operations, a particular electron spin arrangement in periodic 1D (the Lloyd model test bed [19]) etc. Also, from the theoretical viewpoint, heat-bath algorithmic cooling [30] and adiabatic quantum computing [32] by using molecular spins have been proposed. Most of these results were underlain by tailored molecular designs and syntheses for novel open-shell compounds composed of electron bus qubits and nuclear client qubits.

The recent microwave pulse engineering technique, however, offers much to MSQCs to utilize a global control paradigm instead of the access to individual spins. An optimal pulse technique, GRadient Ascent Pulse Engineering (GRAPE) [37], is based on dynamical simulations of spins and suggests that the optimal waveform of irradiation pulses applied to spin systems can afford an efficient execution of quantum simulations. This approach no longer requires individual manipulations of molecular spins to perform quantum gates. As exemplified here, the optimal microwave pulses are capable of controlling nuclear spin states via electron spins in the solid state. This is the essential part to fully control molecular spin qubit systems only by using the microwave pulses. Thus, we have studied for the first time how to perform particular quantum gates in molecular spin qubits in terms of the global control paradigm, and the findings here are relevant to synthetic strategies to realize QCs with more spin qubits in the global control paradigm.

In this work, we have focused on the indirect control of nuclear spin qubits by the microwave optimal pulse irradiation. The molecular spin systems under study, both potassium hydrogen maleate (KHM) and ^{13}C- labeled malonyl radicals, have one electron and two nuclear spin qubits which are coupled with highly anisotropic hyperfine tensors. These molecules have salient features of spin interactions and selected as realistic test beds to execute gate operations. KHM radical has hydrogen homonuclear qubits with symmetrical hyperfine principal values arising from its molecular steric structure. On the other hand, malonyl radical has hydrogen and carbon heteronuclear qubits, where their hyperfine tensors are nearly collinear. In order to figure out their gate control accuracy (fidelity) and what factors govern the fidelity, we have estimated computational performance of the two MSQCs taking account of the controllability of quantum gates, noting that the full controllability is requisites to perform universal quantum gates.

The optimal microwave pulse and relevant gate fidelity were calculated on the basis of the GRAPE approach with scanning the static magnetic field (B_0) direction with respect to the molecular axes, quantitatively sorting out the directional features of the fidelity. Throughout this work, the orientation study is based on the fact that the spin Hamiltonian tensors depending on the B_0 direction make the controllability governed, and thus we can find intrinsic conditions relevant to the feasibility of the magnetic tensors to use for MSQCs. These calculations were invoked only in three quantum gates between the hyperfine qubits, e.g., two CNOT gates and one SWAP gate, which are the most

important for implementing QCs.

As a result, the fidelity in each orientation shows a clear correlation between the controllability and the features of hyperfine tensors. The controllability is governed by a mechanism relevant to the Lie algebra generated by spin Hamiltonians, which fully describe the multiple spin states. Experimentally, the microwave pulse manipulates hyperfine qubits via the anisotropy of their hyperfine interactions connecting the three spin qubits, and then the spin system acquires the full controllability. Thus, the molecular spin system featuring in strong hyperfine anisotropy is suitable for the optimal control. Furthermore, we have found that there are particular orientations which are unfeasible to render nuclear spins controlled, when the relevant hyperfine anisotropy vanishes, i.e. those along the principal axes of the hyperfine tensors. Generally, off-principal axis orientations are further away from those directions, the higher control accuracies acquired. This suggests that the fully co-axial or collinear properties of the hyperfine tensors are favored for hyperfine qubits to serve as MSQCs such as ^{13}C-labeled malonyl radical. This also implies that the knowledge relevant to the molecular optimizations for the quantum control entails useful molecular designs or synthetic strategies for realistic MSQCs with more available qubits.

The present study of the orientation relevant to the hyperfine anisotropy suggests that qubit distinguishability can affect the full controllability in molecular spins. This finding has appeared in the QC experiment on KHM radical in a straightforward manner. The experiment illustrates that the homonuclear qubits lack the distinguishability in terms of the symmetry of their hyperfine tensors, suggesting that qubit distinguishability in molecular designs or optimizations is essential and that highly symmetric molecular designing should be avoided except for molecular optimizations for particular purposes relevant to the creation of highly degenerate nuclear spin states [51].

As described above, we have illustrated that the GRAPE approach based on microwave irradiation can be a powerful tool for quantum control of nuclear spin sates in MSQCs if elaborately selecting the orientations of the static magnetic field. In this approach, the hyperfine tensor properties such as its anisotropy, symmetry and nuclear species are the key to success of the molecular design and optimization for MSQCs. We note that this approach can afford only the first attempt to discuss a strong correlation between the controllability of nuclear spin states and the spin dynamics of the system when the optimal pulses of microwave are irradiated. We expect that the findings in this study will serve as guidelines to improve quantum control theories, experimental implementations and to perform time-consuming syntheses of novel MSQCs.

4. Conclusions

Quantum state control is one of the most important concepts in advanced quantum technology, emerging quantum cybernetics and related fields. In this work, the effect of molecular characteristics on indirect quantum control of nuclear spin states in molecular spin qubits such as realistic hyperfine qubits has been dealt with. In our scenario of three-spin systems under study, microwave pulses are applied to the unpaired electron spin only, i.e. a bus qubit and two hyperfine qubits are indirectly controlled through their hyperfine interaction. Our analysis here shows that the controllability of the

spin system largely depends on the molecular orientation (with respect to the static magnetic field) as well as the symmetry of the hyperfine tensors of the nuclear spin qubits. For the three spin qubit systems under study, the hyperfine qubits are fully controllable, and the optimal microwave pulses are implemented. Thus, we suggest guidelines for molecular optimization which enables us to identify preferable orientations of the static magnetic field with respect to the magnetic tensors of molecular spin qubits and to design molecular spin qubits suitable for executing indirect quantum control. To our knowledge, this exemplifies the first attempt to achieve quantum control by using realistic molecular spin qubits.

We have chosen two molecular spin qubits as a test bed for implementing molecular spin based quantum control, i.e. KHM radical and ^{13}C-labeled malonyl radical in their crystal. The comparison between the two representative molecular spins in terms of molecular characteristics implies that malonyl radical is more suitable for the quantum control than KHM radical. This is because both the client nuclear qubits of malonyl radical, i.e. the α-proton and ^{13}C nucleus, share essentially the same principal axes of the hyperfine tensors and the collinearity of the hyperfine tensors minimizes the probability occurrence of simultaneous uncontrollability of the two client qubits. Moreover, the distinguishability between the two hyperfine qubits also helps entail the individual controllability via the electron spin as the bus qubit.

Unlike malonyl radical, the hyperfine tensors of the two α-protons in KHM radical are of symmetric configuration and they share only one co-principal axis. This particular molecular feature makes it more difficult to differentiate between the two hyperfine qubits and thus leads to the lower fidelity of the gate operations.

The comprehensive numerical analyses in this work have shown that the overall gate fidelity is higher when the static magnetic field is applied in the direction far from the principal axes of the hyperfine tensors of the nuclear client qubits. This appears to be a generic feature and has been interpreted qualitatively. The findings in this work give useful guidelines for molecular designs and molecular optimization of molecular spin based qubits, which enable us to implement quantum control utilizing a more number of hyperfine qubits for more complex series of gate operations.

The GRAPE experiments on other types of molecular spin qubits are underway. Indirect detection in the scheme of an electron spin nutation technique and time trace of the electron spin state are planned in order to get further insights into the quantum control in molecular spin systems. The approach can supply information on the nuclear spin states by back interaction to the electron. Practically, we also plan to carry out direct detections [25] by the use of rectangular and GRAPE pulses.

It is worth noting that molecular spin-based quantum computers (MSQCs) such as malonyl radical, which is composed of one electron spin bus qubit and multiple nuclear spin client qubits in ensemble, have an intrinsic disadvantage to qubit initialization due to small spin energy gaps of the system. This is the reason why MSQCs in ensemble require gate operations at low temperature such as below 2 K, e.g. at W-band experiments for malonyl radical under high static magnetic fields. In order to overcome this disadvantage, a pseudo-pure electron nuclear spin state of malonyl radical in the crystal was generated and the entanglement between an electron spin and a spin-1/2 nuclear spin (α-proton) was for the first time demonstrated [52]. The pseudo-initialization method, which is underlain

by the creation of pseudo-pure electron-nuclear spin states, invokes a particular spin relaxation undergone in the malonyl radical system. On the other hand, another approach to establish qubit initialization for MSQCs is to exploit heat-bath algorithmic cooling at elevated temperature, and an experimental attempt to use ^{13}C-labeled malonyl radical in the crystal has been carried out [30], in which pulsed radio-frequencies have been applied to directly manipulate the nuclear spin client qubits at X-band microwave frequency experiments. In the algorithmic cooling experiment, full information on spin relaxations entailed in the crystal system are essential in addition to the complete sets of its spin-Hamiltonian parameters. We plan to carry out quantum computing experiments and simulations by exploiting the indirect manipulation of the nuclear client qubits in the three-spin qubit system of malonyl radical, in which its spin relaxations in the crystal are taken into account at both X- and Q-band microwave frequencies. To avoid sensitivity reduction due to microwave power saturation effects of the system occurring at low temperature, transmission spectroscopy in the dispersive regime is considered [53].

We have shown that insights from the general theory of quantum control are useful and the application to realistic molecular spins as a test bed can afford relevant quantitative analyses, which entail any further necessary molecular optimization of molecular spin qubits for quantum information processing.

Conflicts of interest
There are no conflicts of interest to declare.

Acknowledgments

Notes and references

1   M. A. Nielsen and I. L. Chuang, *Quantum Computation and Quantum Information* (Cambridge University Press, 2000)

2   A. Aspuru-Guzik, A. D. Dutoi, P. J. Love and M. Head-Gordon, Simulated quantum computation of molecular energies. Science **309**, 1704–1707 (2005)

3   D, S. Abrams and S. Lloyd, Quantum algorithm providing exponential speed increase for finding eigenvalues and eigenvectors. Phys. Rev. Lett. **83**, 5162–5165 (1996)

4   K. Sugisaki, S. Yamamoto, S. Nakazawa, K. Toyota, K. Sato, D. Shiomi and T. Takui, Quantum Chemistry on Quantum Computers: A Polynomial-Time Quantum Algorithm for

Constructing the Wave Functions of Open-Shell Molecules, J. Phys. Chem. A. **120**, 6459-6466 (2016)

5   T. D. Ladd, F. Jelezko, R. Laflamme, Y. Nakamura, C. Monroe and J. L. O'Brien, Quantum Computers, Nature **464**, 45-53 (2010)

6   S. Barz, E. Kashefi, A. Broadbent, J. F. Fitzsimons, A. Zeilinger and P. Walther, Demonstration of Blind Quantum Computing, Science **335**, 303-308 (2012)

7   B. P. Lanyon, C. Hempel, D. Nigg, M. Muller, R. Gerritsma, F. Zahringer, P. Schindier, J. T. Barreiro, M. Rambach, G. Kirchmair, M. Hennrich, P. Zoller, R. Blatt and C. F. Roos, Universal Digital Quantum Simulation with Trapped Ions, Science **334**, 57-61 (2011)

8   N. Timoney, I. Baumgart, M. Johanning, A. F. Varon, M. B. Plenio, A. Retzker and C. Wunderlich, Quantum Gates and Memory Using Microwave-Dressed States, Nature **476**, 185-188 (2011)

9   J. T. Barreiro, M. Muller, P. Schindler, D. Nigg, T. Monz, M. Chwalla, M. Hennrich, C. F. Roos, P. Zoller and R. Blatt, An Open-system Quantum Simulator with Trapped Ions, Nature **470**, 486-491 (2011)

10 J. A. Jones, M. Mosca and R. H. Hansen, Implementation of a Quantum Search Algorithm on a Quantum Computer, Nature **393**, 344-346 (1998)

11 L. M. K. Vandersypen, M. Steffen, G. Breyta, C. S. Yannoni, M. H. Sherwood and I. L. Chuang, Experimental Realization of Shor's Quantum Factoring Algorithm Using Nuclear Magnetic Resonance, Nature **414**, 883-887 (2001)

12 J. Baugh, O. Moussa, C. A. Ryan, A. Nayak and R. Laflamme, Experimental Implementation of Heat-bath Algorithmic Cooling Using Solid-state Nuclear Magnetic Resonance, Nature **438**, 470-473 (2005).

13 M. Mehring and J. Mende, Spin-bus Concept of Spin Quantum Computing, Phys. Rev. A **73**, 052303 (2006)

14 Y. Nakamura, Y. A. Pashkin and J. S. Tsai, Coherent Control of Macroscopic Quantum States in a Single-Cooper-pair Box, Nature **398**, 786-788 (1999)

15 L. Robledo, L. Childress, H. Bernien, B. Hansen, P. F. A. Alkemade and R. Hanson, High-Fidelity Projective Read-out of a Solid-state Spin Quantum Register, Nature **477**, 574-578 (2011)

16 X. Zhu, Y. W. Zhu, S. Murali, M. D. Stollers and R. S. Ruoff, Coherent Coupling of a Superconducting Flux Qubit to an Electron Spin Ensemble in Diamond, Nature **478**, 221-224 (2011)

17 K. C. Nowack, M. Shafiei, M. Laforest, G. E. D. K. Prawiroatmodjo, L. R. Shreiber, C. Reichi, W. Wegscheider and L. M. K. Vandersypen, Single-Shot Correlations and Two-Qubit Gate of Solid-State Spins, Science **333**, 1269-1272 (2011)

18 *Object-oriented Magnetic Resonance; Classes and Objects, Calculations and Computations*, ed. M. Mehring and V. A. Weberruss (Academic Press, San Diego, 2001)

19 Y. Morita, Y. Yakiyama, S. Nakazawa, T. Murata, T. Ise, D. Hashizume, D. Shiomi, K. Sato,

M. Kitagawa, K. Nakasuji and T. Takui, Triple-Stranded Metallo-Helicates Addressable as Lloyd's Electron Spin Qubits, J. Am. Chem. Soc. **132**, 6944-6946 (2010)

20 H. Atsumi, S. Nakazawa, C. Dohno, K. Sato, T. Takui and K. Nakatani, Ligand-induced Electron Spin-Assembly on a DNA Tile, Chem. Commun **49**, 6370-6372 (2013)

21 S. Yamamoto, S. Nakazawa, K. Sugisaki, K. Maekawa, K. Sato, K. Toyota, D. Shiomi and T. Takui, Structural Determination of a DNA Oligomer for a Molecular Spin Qubit Lloyd Model of Quantum Computers, Z. Physik. Chem. **231**, 439-458 (2016)

22 A. Fernandez, J. Ferrando-Soria, E. M. Pineda, F. Tuna, I. J. Vitorica-Yrezabal, C. Knappke, J. Ujima, C. A. Muryn, G. A. Timco, P. E. Barran, A. Ardavan and R. E. P. Winpenny, Making Hybrid [n]-rotaxanes as Supramolecular Arrays of Molecular Electron Spin Qubits, Nat. Commun. **7**, 10240 (2016)

23 K. Sato, S. Nakazawa, R. Rahimi, T. Ise, S. Nishida, T. Yoshino, N. Mori, K. Toyota, D. Shiomi, Y. Yakiyama, Y. Morita, M. Kitagawa, K. Nakasuji, M. Nakahara, H. Hara, P. Carl, P. Höfer and T. Takui, Molecular Electron-spin Quantum Computers and Quantum Information Processing: Pulse-based Electron Magnetic Resonance Spin Technology Applied to Matter Spin-qubits, J. Mater. Chem. **19**, 3739-3754 (2009)

24 T. Yoshino, S. Nishida, K. Sato, S. Nakazawa, R. D. Rahimi, K. Toyota, D. Shiomi, Y. Morita, M. Kitagawa and T. Takui, ESR and ^{1}H-,^{19}F-ENDOR/TRIPLE Study of Fluorinated Diphenylnitroxides as Synthetic Bus Spin-Qubit Radicals with Client Qubits in Solution, J. Phys. Chem. Lett. **2**, 449–453 (2011)

25 S. Nakazawa, S. Nishida, T. Ise, T. Yoshino, N. Mori, R. Rahimi, K. Sato, Y. Morita, K. Toyota, D. Shiomi, M. Kitagawa, H. Hara, P. Carl, P. Höfer and T. Takui, A Synthetic Two-Spin Quantum Bit: *g*-Engineered Exchange-Coupled Biradical Designed for Controlled-NOT Gate Operations, Angew. Chem. Int. Ed. **124**, 9998-10002 (2012)

26 C. J. Wedge, G. A. Timco, E. T. Spielberg, R. E. George, F. Tuna, S. Rigby, E. J. L. McInnes, R. E. P. Winpenny, S. J. Blundell, A. Ardavan, Chemical Engineering of Molecular Qubits, Phys. Rev. Lett. **108**, 107204 (2012)

27 *Electron Spin Resonance (ESR) Based Quantum Computing, Biological Magnetic Resonance Vol. 31*, ed. T. Takui, L. Berliner, G. Hanson (Springer, New York, 2016)

28 J. J. L. Morton, A. M. Tyryshkin, A. Ardavan, K. Porfyrakis, S. A. Lyon and G. A. D. Briggs, High Fidelity Single Qubit Operations Using Pulsed Electron Paramagnetic Resonance, Phys. Rev. Lett. **95**, 200501 (2005)

29 M. S. Fataftah, J. M. Zadrozny, S. C. Coste, M. J. Graham, D. M. Rogers and D. E. Freedman, Presentation of Membrane-anchored Glycosphingolipids Determined from Molecular Dynamics Simulations and NMR Paramagnetic Relaxation Rate Enhancement, J. Am. Chem. Soc. **138**, 1344-1388 (2016)

30 D. K. Park, G. Feng, R. Rahimi, S. Labruyère, T. Shibata, S. Nakazawa, K. Sato, T. Takui, R. Laflamme and J. Baugh, Hyperfine Spin Qubits in Irradiated Malonic Acid: Heat-bath Algorithmic Cooling, Quantum Inf. Process. **14**, 2435-2461 (2015) DOI: 10.1007/s11128-015-

0985-1.

31 M. Yu. Volkov and K. M. Salikhov, Pulse Protocols for Quantum Computing with Electron Spins as Qubits, Appl. Magn. Reson. **41**, 145-154 (2011)

32 S. Yamamoto, S. Nakazawa, K. Sugisaki, K. Sato, K. Toyota, D. Shiomi and T. Takui, Adiabatic Quantum Computing with Spin Qubits Hosted by Molecules, Phys. Chem. Chem. Phys. **17**, 2742-2749 (2015)

33 P. E. Spindler, Y. Zhang, B. Endeward, N. Gershernzon, T. E. Skinner, S. J. Glaser and T. F. Prisner, Shaped Optimal Control Pulses for Increased Excitation Bandwidth in EPR, J. Magn. Reson. **218**, 49−58 (2012).

34 P. E. Spindler, S. J. Glaser, T. E. Skinner and T. F. Prisner, Broadband Inversion PELDOR Spectroscopy with Partially Adiabatic Shaped Pulses, Angew. Chem., Int. Ed. **52**, 3425−3429 (2013)

35 A. Doll and G. Jeschke, Fourier-transform Electron Spin Resonance with Bandwidth-Compensated Chirp Pulses, J. Magn. Reson. **246**, 18−26 (2014)

36 D. Tannor, V. Kazakov and V. Orlov, in *Time Dependent Quantum Molecular Dynamics*, ed. J. Broeckhove and L. Lathouwers (NATO ASI, Ser. B, Plenum, New York, 1992)

37 N. Khaneja, T. Reiss, C. Kehlet, T. Schulte-Herbrüggen and S. J. Glaser, Optimal Control of Coupled Spin Dynamics: Design of NMR Pulse Sequences by Gradient Ascent Algorithms, J. Magn. Reson. **172**. 296-305 (2005)

38 Z. Wu, J. Li, W. Zheng, J. Luo, M. Feng and X. Peng, Experimental Demonstration of the Deutsch-Jozsa Algorithm in Homonuclear Multispin Systems, Phys. Rev. A **84**, 042312 (2011)

39 N. Xu, J. Zhu, D. Lu, X. Zhou, X. Peng and J. Du, Quantum Factorization of 143 on a Dipolar-Coupling Nuclear Magnetic Resonance System, Phys. Rev. Lett. **108**, 130501 (2012)

40 J. S. Hodges, J. C. Yang, C. Ramanathan and D. G. Cory, Universal Control of Nuclear Spins via Anisotropic Hyperfine Interactions, Phys. Rev. A **78**, 010303 (2008)

41 Y. Zhang, C. A. Ryan, R. Laflamme and J. Baugh, Coherent Control of Two Nuclear Spins Using the Anisotropic Hyperfine Interaction, Phys. Rev. Lett. **107**, 170503 (2011)

42 T. W. Borneman and D. G. Cory, Bandwidth-Limited Control and Ringdown Suppression in High-Q Resonators, arXiv: quantum-ph/1207.1139.

43 S. F. Darlow and W. Cochran, The Crystal Structure of Potassium Hydrogen Maleate, Acta Cryst. **14**, 1250-1257 (1961)

44 T. Cole and C. Heller, Hyperfine Splittings in the $(HOOC)C^{13}H(COOH)$ Radical, J. Chem. Phys. **34**, 1085-1086 (1961)

45 D. D'Alessandro, *Introduction to Quantum Control and Dynamics* (Taylor and Francis, Boca Raton, FL, 2008)

46 D. Burgarth, K. Maruyama, M. Murphy, S. Montangero, T. Calarco, F. Nori and M. B. Plenio, Scalable Quantum Computation via Local Control of Only Two Qubits, Phys. Rev. A. **81**, 040303 (2010)

47 J. S. Hodges, J. C. Yang, C. Ramanathan and D. G. Cory, Universal Control of Nuclear Spins

via Anisotropic Hyperfine Interactions, Phys. Rev. A **78,** 010303 (2008).

48 S. Machnes, U. Sander, S. J. Glaser, P. de Fouquières, A. Gruslys, S. Schirmer and T. Schulte-Herbrüggen, Comparing, Optimizing, and Benchmarking Quantum-control Algorithms in a Unifying Programming Framework, Phys. Rev. A **84**, 022305 (2011).

49 J. Nocedal and S. J. Wright, *Numerical Optimization 2nd ed*. (Springer, New York, 2006)

50 H. C. Heller and T. Cole, Electron Magnetic Resonance of X-Irradiated Potassium Hydrogen Maleate, J. Am. Chem. Soc. **84**, 4448-4451 (1962).

51 A. Ueda, S. Suzuki, K. Yoshida, K. Fukui, K. Sato, T. Takui, K. Nakasuji, Y. Morita, Hexamethoxyphenalenyl as a Possible Quantum Spin Simulator: An Electronically Stabilized Neutral pi Radical with Novel Quantum Coherence Owing to Extremely High Nuclear Spin Degeneracy, Angew. Chemie. Int. Ed. **52**, 4795-4799 (2013).

52 M. Mehring, J. Mende and W. Scherer, Entanglement between an Electron and a Nuclear Spin 1/2, Phys. Rev. Letters 90, 15300 (2003).

53 Claudio Bonizzoni, Alberto Ghirri, Shigeaki Nakazawa, Shinsuke Nishida,Kazunobu Sato, Takeji Takui and Marco Affronte, Transmission Spectroscopy of Molecul;ar Spin Ensembles in the Dispersive Regime, Advanced Quantum Technologies, **2021**. DOI: 10.1002/qute.202100039

ORCID Information:
Kenji Sugisaki; orcid.org/0000-0002-1950-5725
Kazunobu Sato; orcid.org/0000-0003-1274-7470
Takeji Takui; orcid.org/0000-0001-6238-5215

Supplementary Information

Molecular Optimization for Nuclear Spin State Control via A Single Electron Spin Qubit by Optimal Microwave Pulses: Quantum Control of Molecular Spin Qubits

Taiki Shibata,[a] Satoru Yamamoto,[a] Shigeaki Nakazawa,[a, #] Elham Hosseini Lapasar[a, b, *], Kenji Sugisaki,[a, c, d] Koji Maruyama,[a] Kazuo Toyota,[a] Daisuke Shiomi,[a] Kazunobu Sato[a, *] and Takeji Takui[a, e, *]

[a] Department of Chemistry and Molecular Materials Science, Graduate School of Science, Osaka City University, Osaka 558-8585, Japan

[b] Department of Physics, University of Guilan, 41335-1914 Rasht, Iran

[c] JST PRESTO, Saitama 332-0012, Japan

[d] Centre for Quantum Engineering, Research and Education (CQuERE), TCG Centres for Research and Education in Science and Technology (TCG CREST), Kolkata 700091, India

[e] Research Support/URA Center, University Administration Division, Osaka City University, Osaka 558-8585, Japan

 # Deceased on March 23, 2019.

Corresponding author: Takeji Takui

E-mail address of the corresponding author: takui@sci.osaka-cu.ac.jp

Table of Contents

1. One electron and two nuclear spin systems in single crystals

1.1 The hyperfine tensors of protons in KHM radical

Potassium hydrogen maleate (KHM) radical depicted in Fig. S1(a) has been chosen as a test bed for a molecular spin qubit with an one electron and two ^{1}H nuclear spins, in which the two hyperfine qubits are equivalent except for one principal axis of the hyperfine tensors in this work. In the previous studies,[S1, S2] the orthorhombic crystal of the KHM host molecule was reported from the X-ray diffraction measurements, and the ESR spectra of KHM radical generated by γ-/X-ray irradiation showed also the crystal symmetry (Fig. S1(b)). The unit cell contains four molecules and two magnetically non-equivalent orientations for KHM radical, say orientations 1 and 2. The hyperfine tensors of two protons for the orientation 1 in the *abc* orthogonal crystallographic coordinate system are

$$A_{\text{KHM1}}(\text{H2}) = \begin{pmatrix} -14.6 & -3.7 & 7.4 \\ -3.7 & -16.0 & -6.3 \\ 7.4 & -6.3 & -23.0 \end{pmatrix} \text{MHz} \qquad \text{(hf-1a)}$$

$$A_{\text{KHM1}}(\text{H3}) = \begin{pmatrix} -14.6 & -3.7 & -7.4 \\ -3.7 & -16.0 & 6.3 \\ -7.4 & 6.3 & -23.0 \end{pmatrix} \text{MHz} \qquad \text{(hf-1b)}$$

and those for the orientation 2 are

$$A_{\text{KHM2}}(\text{H2}) = \begin{pmatrix} -14.6 & 3.7 & -7.4 \\ 3.7 & -16.0 & -6.3 \\ -7.4 & -6.3 & -23.0 \end{pmatrix} \text{MHz} \qquad \text{(hf-2a)}$$

$$A_{\text{KHM1}}(\text{H3}) = \begin{pmatrix} -14.6 & 3.7 & 7.4 \\ 3.7 & -16.0 & 6.3 \\ 7.4 & 6.3 & -23.0 \end{pmatrix} \text{MHz} \qquad \text{(hf-2b).}$$

The difference between hf-1 and hf-2 is a sign of off-diagonal elements of the hyperfine tensors. In

the manuscript, we consider the orientation 1 for our purpose and simplicity. The electron spin, ^{1}H2 and ^{1}H3 nuclear spins with the parameter set of hf-1 are named the 1st, 2nd and 3rd qubits, respectively in the present molecular spin qubits. The nuclear spins are termed hyperfine qubits.
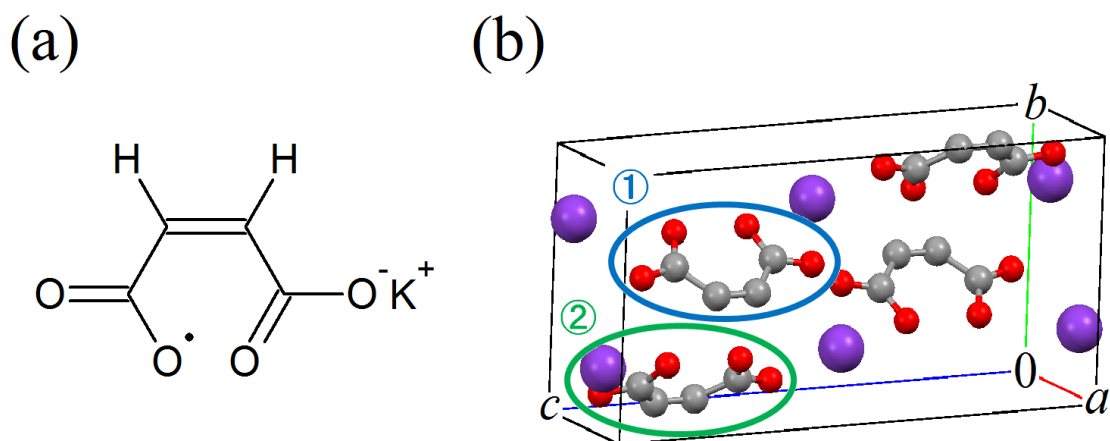

Figure S1 The molecular and crystal structures of KHM radical (a) The molecular structure of KHM radical. (b) The crystal structure of KHM radical in the *abc* crystallographic coordinate system defined as the molecular coordinate (*xyz*) system, reported by the X-ray diffraction study. Atoms, ^{16}O, ^{12}C and ^{39}K atoms are denoted in red, gray and purple spheres, respectively. The orientation 1 and 2 are circled in blue and green, respectively. Note that the true molecular structure of KHM radical in the crystal lattice of the KHM host molecule has not experimentally been determined yet, and speaking exactly the structure have only been suggested by ESR spectroscopy and relevant theoretical considerations.

1.2 The hyperfine tensors of the α-proton and ^{13}C-labeled nucleus in ^{13}C- labeled malonyl radical

The ^{13}C- labeled malonyl radical depicted in Fig. S2 has been utilized for a hyperfine qubit with heteronuclear spin system which is composed of one electron spin (1st), ^{1}H nuclear (2nd) and ^{13}C (3rd) nuclear client spin qubits. Since the crystal of malonic acid having malonyl radical is triclinic, there is only one molecular orientation.[S3] From the experimental point of view, any precise orientation of the static magnetic field with respect to the triclinic crystallographic coordinate system (*abc*) is very difficult without a proper reference crystal composed of a certain stable open-shell entities with a well-defined large hyperfine anisotropic tensor. Thus, we have chosen a crystallographic orthogonal coordinate system defined in the crystal of malonic acid. The hyperfine tensors of the ^{1}H and ^{13}C hyperfine qubits in the crystallographic orthogonal coordinate system defined in the experiment are

$$A_{mal}(^1H) = \begin{pmatrix} -56.0 & 0.0 & 0.0 \\ 0.0 & -91.5 & 0.0 \\ 0.0 & 0.0 & -26.6 \end{pmatrix} MHz \qquad \text{(hf-3a)}$$

$$A_{mal}(^{13}C) = \begin{pmatrix} 211.8 & 1.0 & -8.9 \\ 1.0 & 24.6 & -1.3 \\ -8.9 & -1.3 & 43.4 \end{pmatrix} MHz \qquad \text{(hf-3b)}.$$
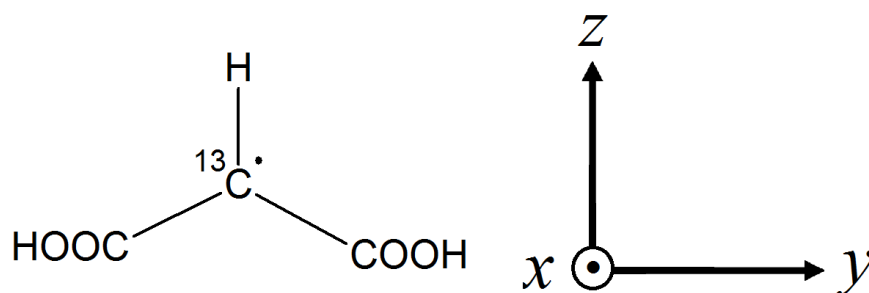

Figure S2 The molecular structure of ^{13}C- labeled malonyl radical. The molecular coordinates (*xyz*) system is defined as the principal axes of the hyperfine tensor for the α-proton. The principal axes of the hyperfine tensor for the ^{13}C nucleus are approximately collinear with the *xyz* axes.

2. Fidelity of GRAPE pulses as a function of physical and operational parameters

Here, we discuss how physical or operational parameters affect quantum gate fidelity of GRadient Ascent Pulse Engineering (GRAPE) pulses. We focus on the CNOT1 gate operation only. The other operations are given in the manuscript.

$$\text{CNOT1} = \begin{pmatrix} 1 & 0 & 0 & 0 & 0 & 0 & 0 & 0 \\ 0 & 1 & 0 & 0 & 0 & 0 & 0 & 0 \\ 0 & 0 & 0 & 1 & 0 & 0 & 0 & 0 \\ 0 & 0 & 1 & 0 & 0 & 0 & 0 & 0 \\ 0 & 0 & 0 & 0 & 1 & 0 & 0 & 0 \\ 0 & 0 & 0 & 0 & 0 & 1 & 0 & 0 \\ 0 & 0 & 0 & 0 & 0 & 0 & 0 & 1 \\ 0 & 0 & 0 & 0 & 0 & 0 & 1 & 0 \end{pmatrix} \qquad \text{(CNOT1)}.$$

The GRAPE pulse and its fidelity are numerically calculated by the DYNAMO toolbox[S5] running on MATLAB software. The calculated fidelity is plotted as a function of the direction of the static magnetic field (B_0) defined with respect to the molecular coordinate (*xyz*) system. In the following section, we define the reference condition (section 2.1) to discuss the fidelity as a functions of magnitudes of the static magnetic field (section 2.2), offset microwave frequency (section 2.3) and operation time (section 2.4).

2.1 Plots of fidelity foe the reference condition.

The set of the physical parameters for the reference condition is set to be the same as in the manuscript. Those are listed in Table S1. The two reference sphere plots in Figs. S3a and S3b, have the same fidelity values for KHM and malonyl radicals as depicted in the manuscript of Fig. 2a and 3a, respectively.

Table S1 The reference condition of the numerical calculations for GRAPE pulses.

Magnitude of B_0	1.1 T (Q-band)
Offset frequency (Δv_0)	10 MHz
Computational time step (Δt)	5 ns
Operation time (KHM radical)	0.5 μs
Operation time (malonyl radical)	0.3 μs
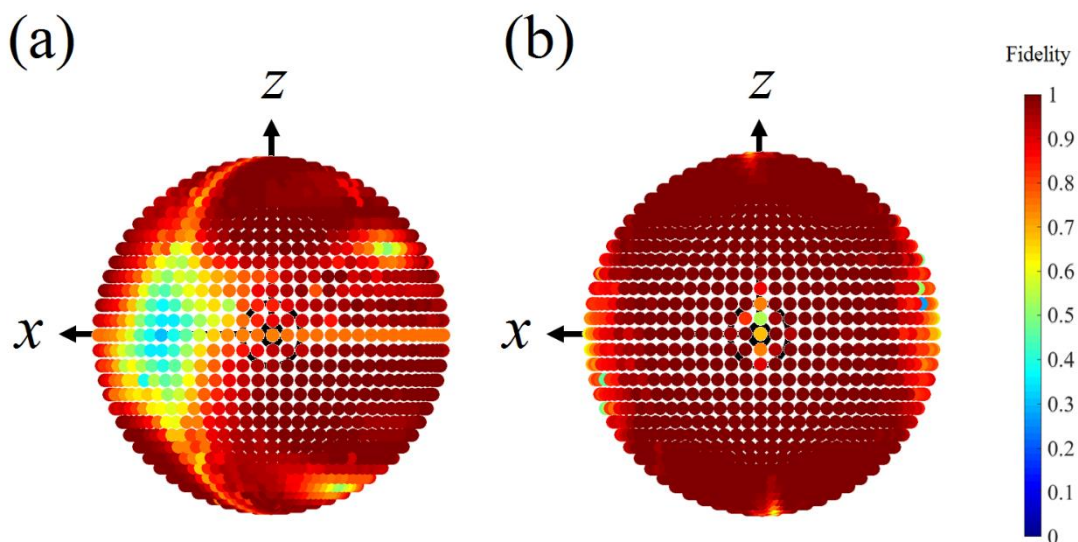
Figure S3 Plots of fidelity for the reference condition. Each colored point in the molecular coordinate (*xyz*) system shows the fidelity as a function of the direction of the static magnetic field (B_0) from the center. (a) KHM radical. (b) ^{13}C-labeled malonyl radical.

2.2 Plots of fidelity for different magnetic field strengths

The B_0 dependence of fidelity is estimated by assuming typically 0.1 T (L-band) and 0.35 T (X-band) in Fig S4 and S5, respectively. The other parameters are set to be the same as the reference condition as listed in Table S1. The two figures show considerably lower fidelity in most orientations compared with those for the reference condition (Q-band) of Fig. S3.
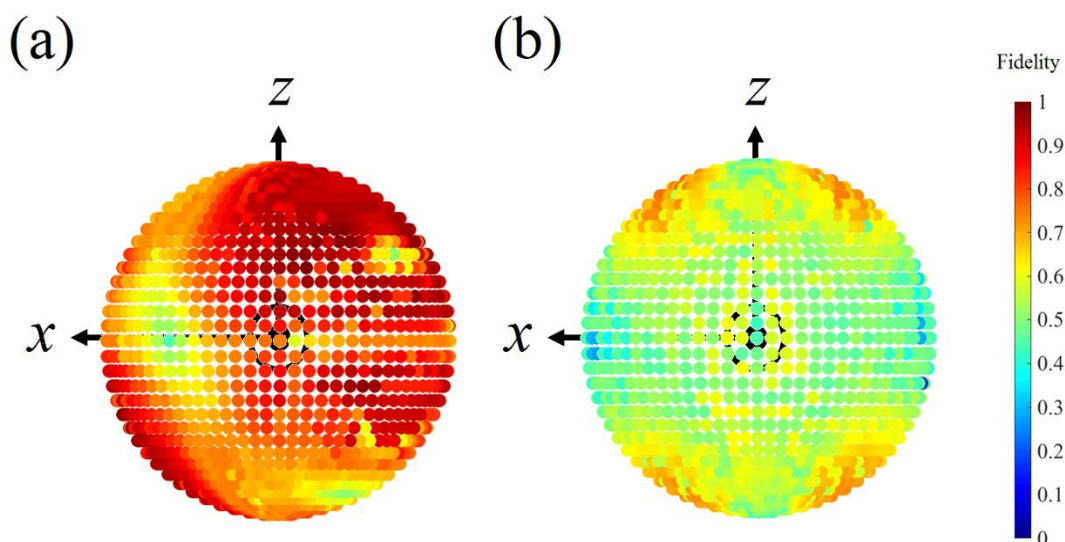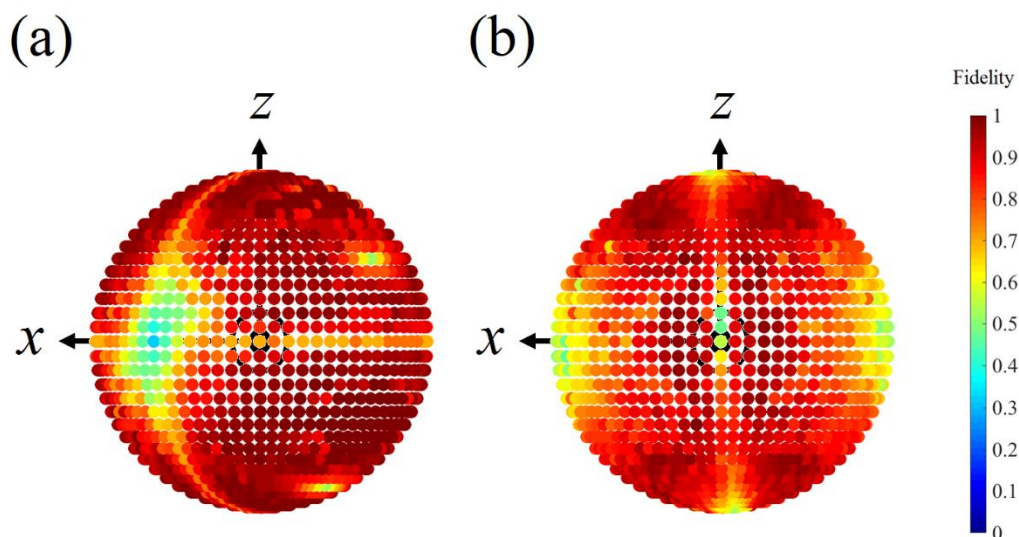

Figure S4 Plots of fidelity for an L-band spectrometer. Each colored points in the molecular coordinate (*xyz*) system shows the fidelity as a function of the direction of the static magnetic field (B_0) from the center. (a) KHM radical. (b) ^{13}C-labeled malonyl radical.

Figure S5 Plots of fidelity for an X-band spectrometer. Each colored point in the molecular coordinate (*xyz*) shows the fidelity with the direction of the static magnetic field (B_0) from the center. (a) KHM radical. (b) ^{13}C-labeled malonyl radical.

2.3 Plots of fidelity for different offset frequency of microwave

We have numerically calculated the GRAPE pulse at the 0 MHz offset microwave frequency. The other parameters are set to be the same as the reference condition, as listed in Table S1. The plots of fidelity are shown in Fig. S6. The fidelity lower than that for the reference condition is obtained.
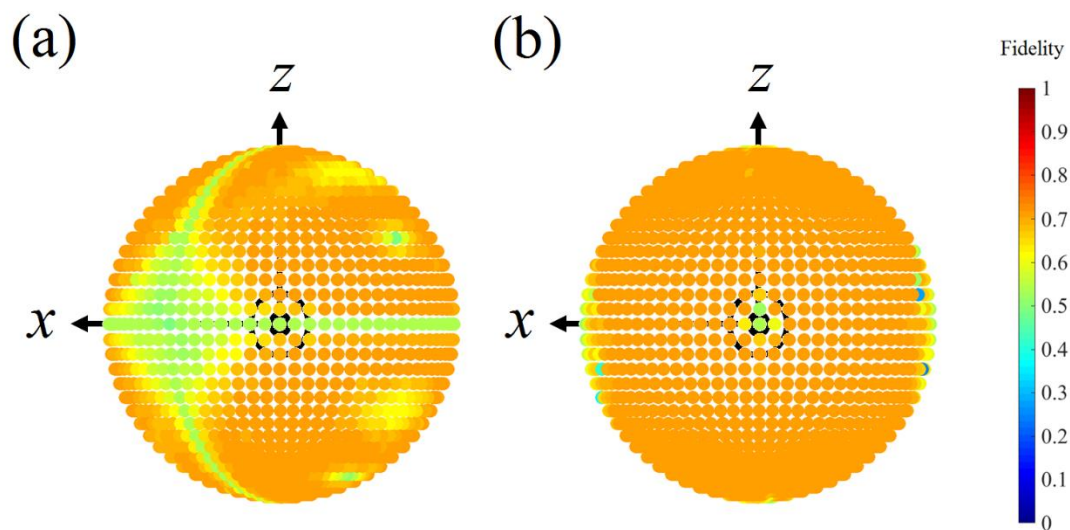

Figure S6 Plots of fidelity at the 0 MHz offset microwave frequency. Each colored point in the molecular coordinate (*xyz*) system shows the fidelity as a function of the direction of the static magnetic field (B_0) from the center. (a) KHM radical. (b) ^{13}C-labeled malonyl radical.

2.4 Plots of fidelity at long operation time.

We have also calculated the GRAPE pulse for the larger operation time (= 1.2 μs) than the reference condition. Physical parameters except for the operation time are set to be the same for the reference condition, as listed in Table S1. The plots of fidelity is shown in Fig. S7. The fidelity is higher than that for the reference condition except for particular molecular orientations being lack of complete controllability. This suggests that the correlation between the fidelity and the corresponding molecular orientation holds when varying the operation time.
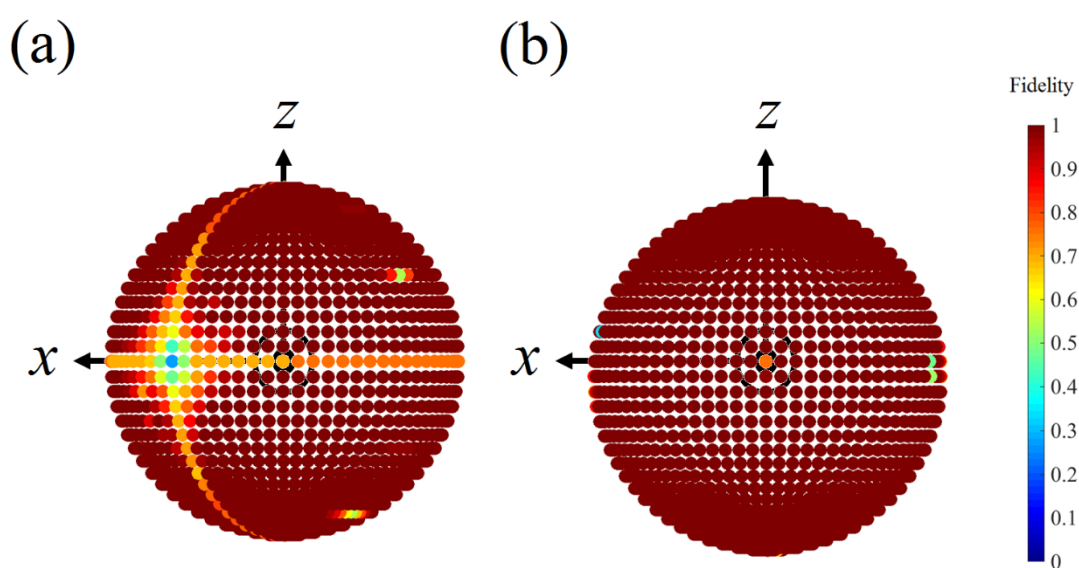
Figure S7 Plots of fidelity at long operation time. The operation time of KHM radical and ^{13}C-labeled malonyl radical is set to be 1.2 μs. Each colored point in the molecular coordinate (*xyz*) system shows the fidelity as a function of the direction of the static magnetic field (B_0) from the center. (a) KHM radical. (b) ^{13}C-labeled malonyl radical.

3. Pulse sequence of GRAPE pulses.

Here, we show the suitable molecular orientations and the pulse sequences for GRAPE pulses acting on the CNOT1 gate. The molecular orientations being far from the low fidelity orientations were carefully selected as discussed in the manuscript. In the following subsection, the physical parameters are fixed as listed in Table S2.

Table S2 The fixed parameters in the GRAPE calculations.

Magnitude of B_0	1.1 T (Q-band)
Offset frequency (Δv_0)	10 MHz
Computational time step (Δt)	5 ns

3.1 Pulse sequences for KHM radical.

The GRAPE pulses for KHM radical have numerically been calculated for the most suitable molecular orientation ($\varphi = 10°$, $\theta = 150°$) depicted in Figs. S8 and S9. Both show high fidelity of 0.99, but with the different operation time. The GRAPE pulse in Fig. S8 was calculated under the reference condition, i.e. the operation time of 0.5 µs. On the other hand, the GRAPE pulse in Fig. S9 is for the larger operation time of 1.2 µs, leading to the decrease in the control amplitude for the ESR-QC experiments.
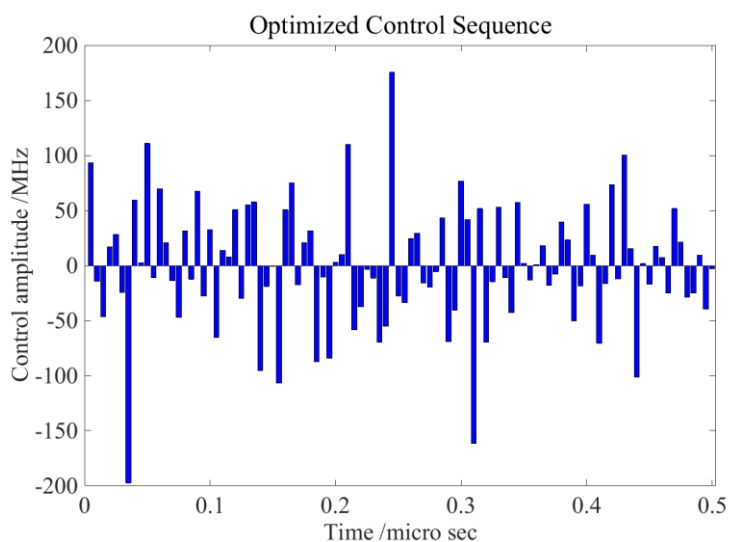
Figure S8 The pulse sequence for KHM radical. The operation time is 0.5 µs (the same as for the reference condition).
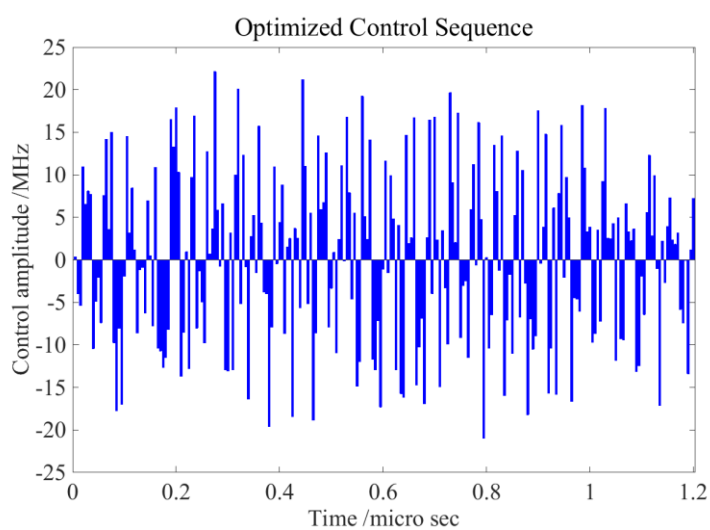

Figure S9 The pulse sequence for KHM radical. The operation time is 1.2 µs, leading to the decrease in the control amplitude.

3.2 Pulse sequences for ^{13}C- labeled malonyl radical.

The GRAPE pulses for ^{13}C- labeled malonyl radical have numerically calculated for the most suitable molecular orientation ($\varphi = 45°$, $\theta = 45°$) depicted in Figs. S10 and Fig. S11. These figures are the same as in Figs. 4c and 4d in the manuscript. Both show high fidelity of 0.99, but for the different operation time. The GRAPE pulse in Fig. S10 was calculated under the reference condition, i.e. the operation time of 0.3 μs. On the other hand, the GRAPE pulse in Fig. S11 is for the larger operation time of 1.2 μs, leading to the decrease in the control amplitude for the ESR-QC experiments.
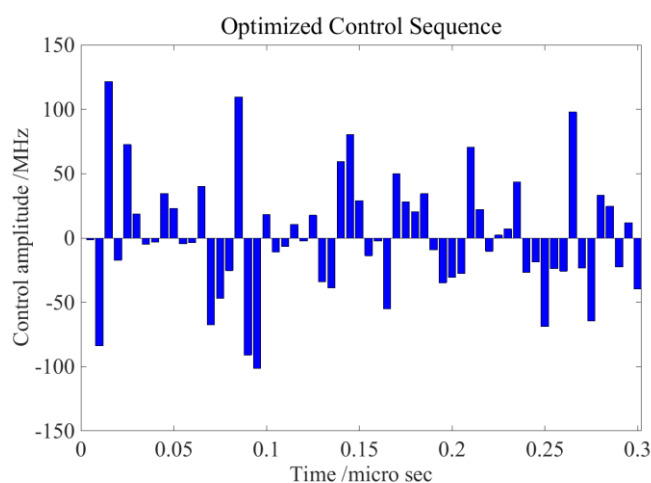

Figure S10 The pulse sequence for ^{13}C- labeled malonyl radical. The operation time is 0.3 μs (the same as for the reference condition).

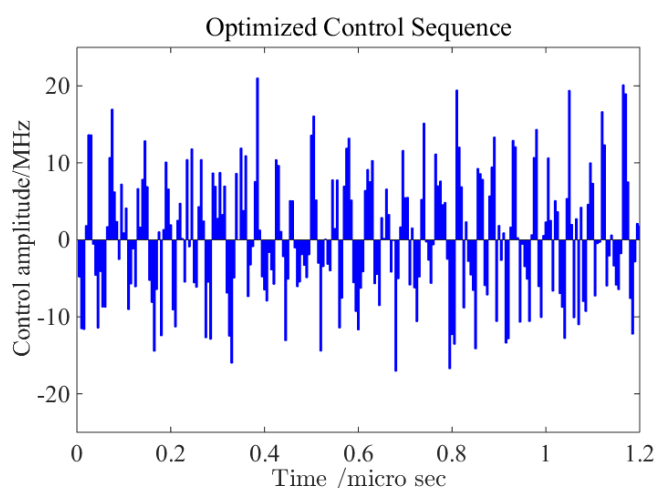**Figure S11** The pulse sequence for ^{13}C- labeled malonyl radical. The operation time is 1.2 μs. leading to the decrease in the control amplitude.

4. The optimized molecular structure of malonyl radical in the host crystal lattice of malonic acid and the spin Hamiltonian parameters for malonyl radical

Speaking exactly, the molecular structure of malonyl radical itself in the host crystal lattice of malonic acid has not fully been determined in its crystal structure, to our knowledge. The optimized molecular structure of malonyl radical in the crystal lattice is given below in detail. The optimized structure of malonyl radical in the crystal lattice has been obtained by considering sixteen host molecules surrounding malonyl radical in the lattice. The optimized structure of malonyl radical obtained in the host crystal is the most probable one theoretically calculated so far.

The target molecular system is malonyl radical with sixteen surrounding closed shell molecules of malonic acid. The geometry optimization was carried out at the level of UB97D/6-31G*. The geometrical parameters of malonyl radical and the two COOH groups of malonic acid those form hydrogen bonds with malonyl radical were optimized. The positions of other atoms were fixed during the geometry optimization. The top and side views of the optimized structure of malonyl radical are given with the sixteen surrounding molecules of malonic acid in Fig. S12.
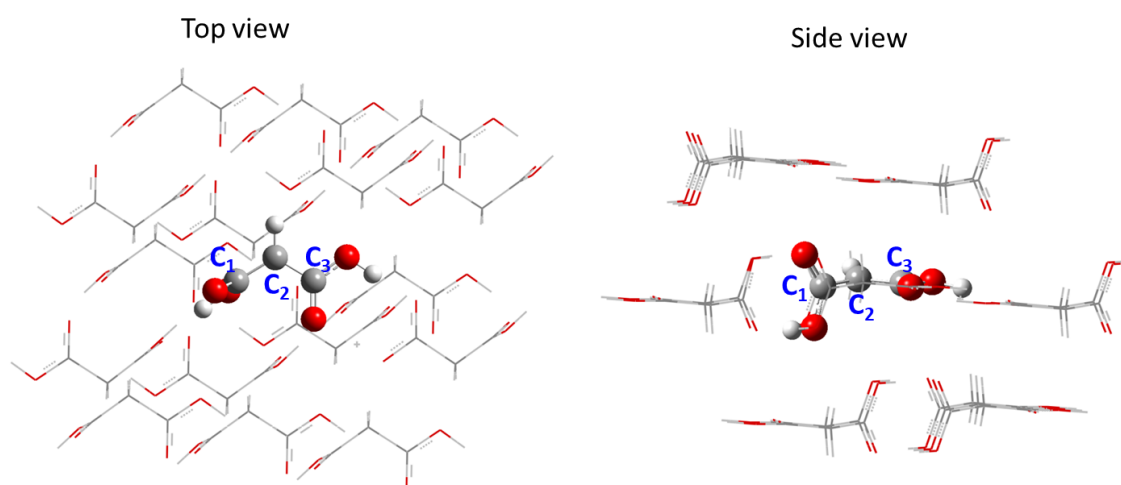

Figure S12 The optimized molecular structure of malonyl radical with sixteen surrounding closed-shell molecules of malonic acid. Ball and stick images denote malonyl radical, and only stick images the closed-shell molecules of malonic acid. Dihedral angles between the central CH and COOH groups are measured by $H-C_2-C_i-OH$: $D(H-C_2-C_1-OH) = 106.29$ degrees, $D(H-C_2-C_3-OH) = -14.44$ degrees.

It is worth noting that the optimized molecular structure reproduces the experimentally determined hyperfine tensors for the 13-carbon atoms and α-proton of the central carbon. The calculated hyperfine tensors (at the UB97D/6-31G* level) for the C_1, C_2 (central carbon), and C_3

atoms, and the α-proton are given in Fig. S13. The spin density plot (isosurface value = 0.005) of malonyl radaical in the crystal, as calculated at the UB97D/6-31G* level is given in Fig. S14.

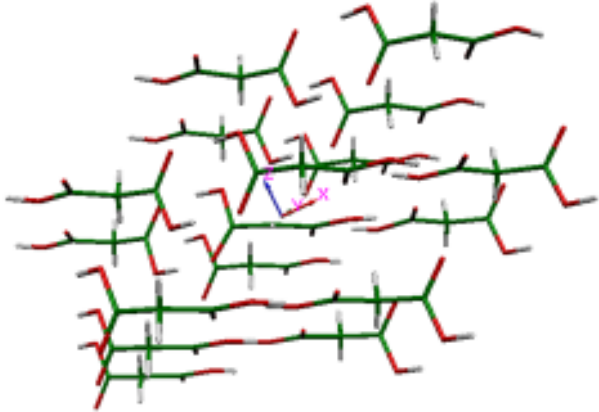Results: Hyperfine tensors (UB97D/6-31G* level)

C1

A_{xx} = -37.655 MHz
A_{yy} = -33.841 MHz
A_{zz} = -32.208 MHz

Direction cosine

0.0087 0.9421 -0.3352
0.5812 0.2680 0.7683
0.8137 -0.2015 -0.5452

C3

A_{xx} = -36.130 MHz
A_{yy} = -35.331 MHz
A_{zz} = -32.066 MHz

Direction cosine

-0.1304 0.6380 0.7589
0.9245 -0.1983 0.3255
0.3582 0.7441 -0.5640

C2 (central carbon)

A_{xx} = 31.417 MHz
A_{yy} = 31.824 MHz
A_{zz} = 226.29 MHz

Direction cosine

0.8816 0.0729 -0.4663
-0.1325 0.9865 -0.0962
0.4530 0.1466 0.8794

H

A_{xx} = -98.803 MHz
A_{yy} = -72.293 MHz
A_{zz} = -26.940 MHz

Direction cosine

0.8548 0.2388 -0.4608
0.4395 0.1394 0.8874
-0.2762 0.9610 -0.0142

Figure S13 The hyperfine tensors calculated at the level of UB97D/6-31G* for the C_1, C_2 (central carbon), and C_3 atoms, and the α-proton are given.
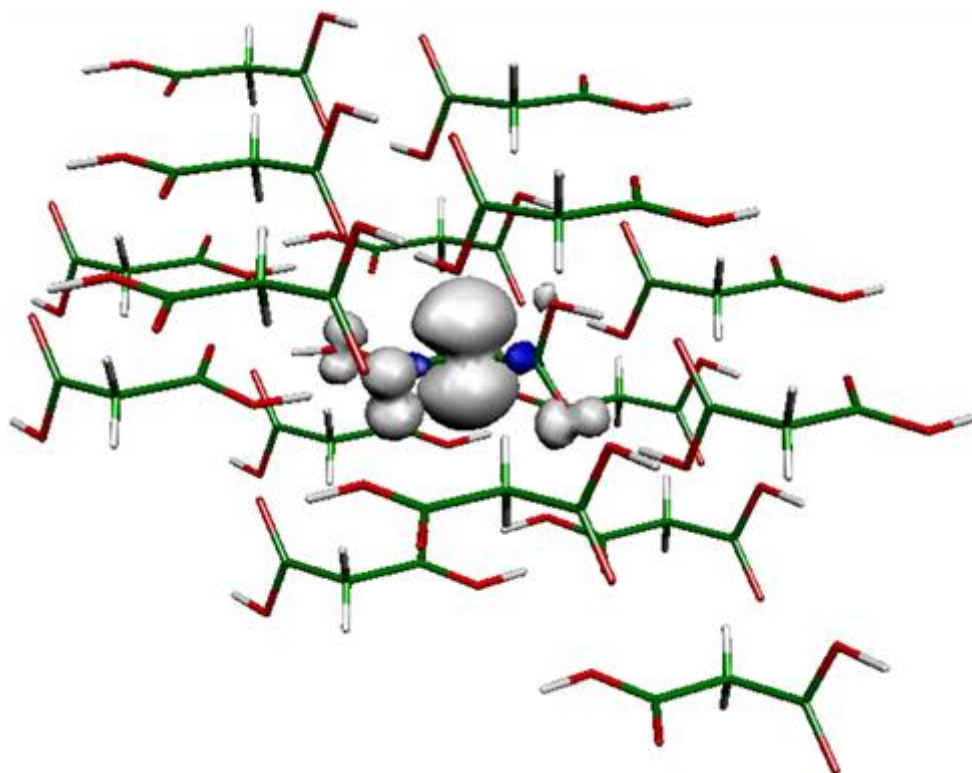
Figure S14 The spin density plot (isosurface value = 0.005) of malonyl radaical in the crystal, as calculated at the UB97D/6-31G* level is given.

Also, the calculated hyperfine tensors (at the UB97D/EPR-II level, geometry-optimized at UB97-D/6-31G*) for the C_1, C_2 (central carbon), and C_3 atoms, and the α-proton are given in Fig. S15. The principal values of the theoretically calculated hyperfine tensors at EPR-II are overestimated.
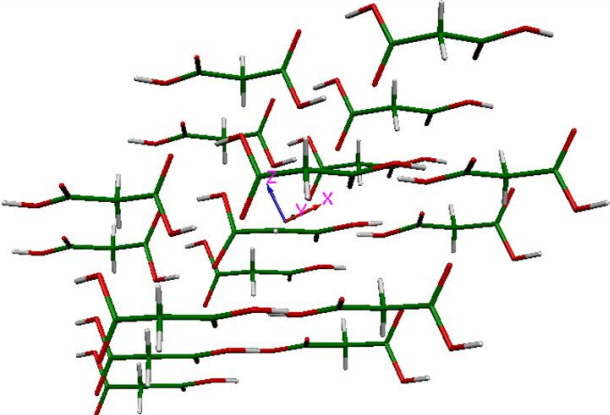
C1

A_{xx} = -51.875 MHz
A_{yy} = -48.064 MHz
A_{zz} = -46.321 MHz

Direction cosine

0.0055 0.9418 -0.3362
0.5727 0.2726 0.7731
0.8197 -0.1968 -0.5379

C3

A_{xx} = -51.196 MHz
A_{yy} = -50.523 MHz
A_{zz} = -47.115 MHz

Direction cosine

-0.3034 0.6805 0.6670
0.8771 -0.0741 0.4745
0.3723 0.7290 -0.5744

C2 (central carbon)

A_{xx} = 66.292 MHz
A_{yy} = 67.345 MHz
A_{zz} = 270.529 MHz

Direction cosine

0.8581 0.1991 -0.4732
-0.2448 0.9689 -0.0362
0.4513 0.1469 0.8802

H

A_{xx} = -98.622 MHz
A_{yy} = -69.467 MHz
A_{zz} = -24.304 MHz

Direction cosine

0.8551 0.2378 -0.4606
0.4400 0.1370 0.8875
-0.2742 0.9616 -0.0125

Figure S15 The hyperfine tensors calculated at the level of UB97D/EPR-II (geometry-optimized at UB97-D/6-31G*) for the C_1, C_2 (central carbon), and C_3 atoms, and the α-proton are given.

5. References.

[S1] S. F. Darlow and W. Cochran, Acta Cryst. **14**, 1250-1257 (1961)

[S2] H. C. Heller and T. Cole, J. Am. Chem. Soc. **84**, 4448-4451 (1962)

[S3] D. K. Park, G. Feng, R. Rahimi, S. Labruyère, T. Shibata, S. Nakazawa, K. Sato, T. Takui, R. Laflamme and J. Baugh, Quantum Inf. Process. **14**, 2435-2461 (2015)

[S4] N. Khaneja, T. Reiss, C. Kehlet, T. Schulte-Herbrüggen and S. J. Glaser, J. Magn. Reson. **172**. 296-305 (2005)

[S5] S. Machnes, U. Sander, S. J. Glaser, P. de Fouquières, A. Gruslys, S. Schirmer and T. Schulte-Herbrüggen, Phys. Rev. A **84**, 022305 (2011)